ЖЭТФ, 2012, том 141, вып. 4, стр. 767–777

ELECTRONIC STRUCTURE OF TWO-DIMENSIONAL HEXAGONAL DISELENIDES: CHARGE DENSITY WAVES AND PSEUDOGAP BEHAVIOR

E. Z. Kuchinskii [a*], ***I. A. Nekrasov*** [a**], ***M. V. Sadovskii*** [a,b]

[a] *Institute for Electrophysics, Ural Branch, Russian Academy of Sciences 620016, Ekaterinburg, Russia*

[b] *Institute for Metal Physics, Ural Branch, Russian Academy of Sciences 620219, Ekaterinburg, Russia*

Received June 27, 2011

We theoretically study the electronic structure (spectral functions and Fermi surfaces) of incommensurate pseudogap and charge density wave (CDW) and commensurate CDW phases of quasi-two-dimensional diselenides 2H-$TaSe_2$ and 2H-$NbSe_2$. The incommensurate pseudogap regime is described within the scenario based on short-range-order CDW fluctuations, considered within the static Gaussian random field model. In contrast, e. g., to high-T_c cuprates, layered dichalcogenides have several different CDW scattering vectors and an electronic spectrum with two bands at the Fermi level. For this, we present a theoretical background for the description of multiple scattering processes within a multiple-band electronic spectrum. Theoretical spectral functions and Fermi surfaces thus obtained are compared with recent ARPES experimental data, demonstrating rather good qualitative agreement.

1. INTRODUCTION

Quasi-two-dimensional dichalcogenides TX_2 (T = = Nb, Ta, Mo, Hf; X = S, Se) and their different polymorphic modifications attracted the attention of scientific community long ago [1]. This was connected with (i) early suggestions to seek high-T_c superconductivity in layered compounds and (ii) the discovery of phase transitions with formation of charge density waves (CDW) [1]. In particular, in 2H-$TaSe_2$ (2H means a hexagonal structure with two Ta layers in the unitcell), a second-order transition into the incommensurate CDW phase is observed at the temperature 122.3 K. At 90 K, there is another transition, to a commensurate CDW phase [1, 2]. In 2H-$NbSe_2$, the transition to incommensurate CDW phase occurs at a much lower temperature of 33.5 K [2] and no commensurate CDW phase is observed.

Above the incommensurate CDW transition temperature in these systems, a range of temperatures might exist where short-range order CDW fluctuations with a finite, but sufficiently large, correlation length ξ exist due to the low-dimensional nature of these systems (and in analogy with antiferromagnetic fluctuations in cuprates). This is indeed observed experimentally in angular resolved X-ray photoemission (ARPES) experiments [3–5].

In this paper, we present band structure calculation results for 2H-$TaSe_2$ and 2H-$NbSe_2$ with the analysis of possible topologies of the Fermi surfaces upon doping, showing the possibility of formation of "bone"-like Fermi sheets. We present the details of the theoretical description of multiband electronic multiple scattering on CDWs in multiple-band systems, applied to pseudogap, incommensurate and commensurate CDW phases for both 2H-$TaSe_2$ and 2H-$NbSe_2$. As an outcome, we obtain spectral functions and Fermi surface maps, which are compared with a number of recent ARPES results [3, 4].

2. BAND STRUCTURE

The 2H-TX_2 layered compounds have a hexagonal crystal structure with the space symmetry group

*E-mail: kuchinsk@iep.uran.ru
**E-mail: nekrasov@iep.uran.ru

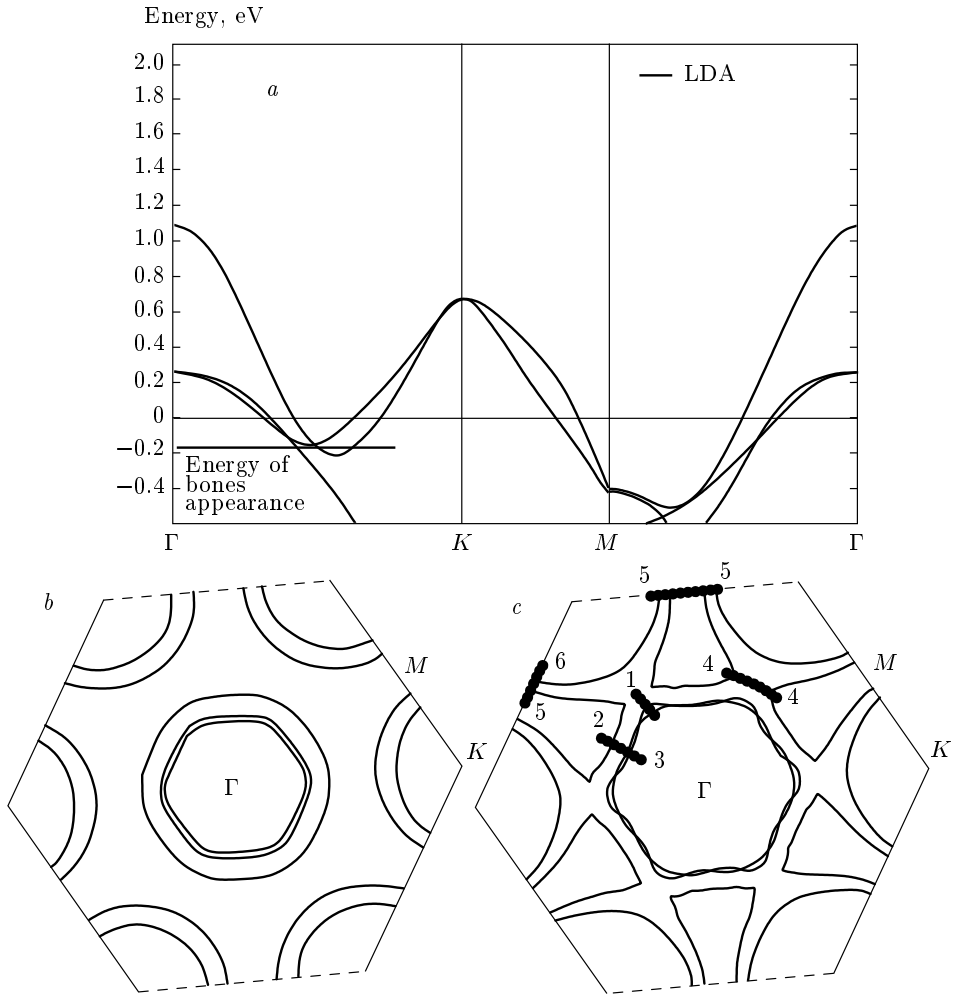

Fig. 1. LDA bands and Fermi surfaces for 2H-$TaSe_2$. Panel (a) — LDA electronic dispersions. The Fermi level corresponds to zero. Panel (b) — the LDA Fermi surface. Panel (c) — the Fermi surface for the Fermi level shown in panel (a) with a short line shifted down to obtain bone-like Fermi sheets

$P6_3/mmc$ with the lattice parameters $a = 3.436$ Å and $c = 12.7$ Å for the Ta system. The corresponding Wyckoff positions are $2b$ (0,0,0.25) for Ta and $4f$ ($\frac{1}{3}$,$\frac{2}{3}$,0.118) for Se [2]. The formal electronic configuration of Ta is d^1. To calculate the electronic structure of the compound, the linearized muffin-tin orbitals method (LMTO) [6] with default settings was used. The obtained band structure and Fermi surfaces are in good agreement with similar LDA calculations by other authors [7]. We do not present any LDA results on 2H-$NbSe_2$ because its crystal structure [2] and the corresponding band structure are very close to those of 2H-$TaSe_2$.

In our LDA calculations, in accordance with the previous works [7], the Fermi level in 2H-$TaSe_2$ is crossed by two Ta-5d bands with the $3z^2 - r^2$ symmetry (see Fig. 1 a), which are well separated from other bands.

The Fermi surface (FS) of 2H-$TaSe_2$ has three (in some works, two [7]) hole-like cylinders near the Γ point and two hole cylinders around the K point. Our results are presented in Fig. 1 b. Here, we observe three hole-like cylinders around the Γ point.

Recently, several ARPES studies detected the experimental FS of 2H-$TaSe_2$. In particular, in Ref. [8], the electronic structure of the valence band was studied in 1T-TaS_2 and 2H-$TaSe_2$. For 2H-$TaSe_2$, it was shown that there are four crossings with the FS along the Γ–K direction. A similar picture is also seen in LDA results (Fig. 1 a,b). In later ARPES studies [3, 4, 9], it was observed that the FS of 2H-$TaSe_2$ has a more complex topology. Namely, "bone"-like FS sheets appear

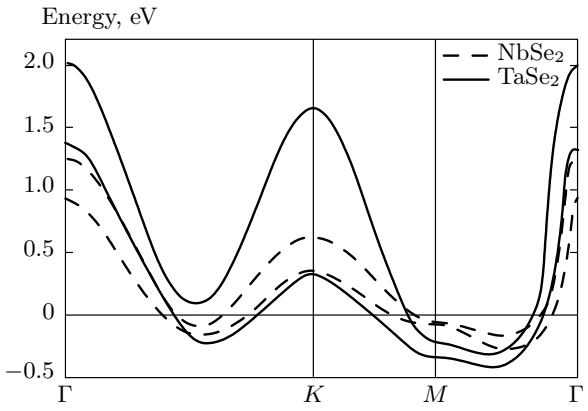

Fig. 2. "Experimental" bands for 2H-$TaSe_2$ (solid lines) and 2H-$NbSe_2$ (dashed lines). The Fermi level corresponds to zero

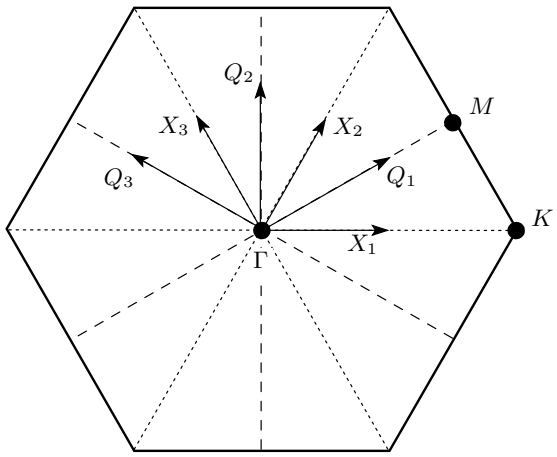

Fig. 3. Schematic picture of the first Brillouin zone for the hexagonal lattice with characteristic CDW vectors: commensurate CDW vectors $\mathbf{Q} = \frac{2}{3}\Gamma M(\mathbf{Q}_1, \mathbf{Q}_2, \mathbf{Q}_3)$ and the vectors $\mathbf{X} = \frac{1}{2}\Gamma K(\mathbf{X}_1, \mathbf{X}_2, \mathbf{X}_3)$ after double scattering on $\mathbf{Q}$, which also have significant Lindhardt function maxima [3]

along the Γ–M direction. Within the LDA picture, such "bones" can be obtained by shifting the Fermi level down by about 0.1 eV (Fig. 1 *a,c*).

In Fig. 2, to improve over simple LDA, we show the "experimental" bands with dispersions:

$$\epsilon(\mathbf{k}) = t_0 + t_1\left[2\cos\frac{k_x}{2}\cos\frac{\sqrt{3}\,k_y}{2} + \cos k_x\right] + t_2\left[2\cos\frac{3k_x}{2}\cos\frac{\sqrt{3}\,k_y}{2} + \cos\sqrt{3}\,k_y\right] + t_3\left[2\cos k_x\cos\sqrt{3}\,k_y + \cos 2k_x\right] + t_4\left[2\cos 3k_x\cos\sqrt{3}\,k_y + \cos 2\sqrt{3}\,k_y\right], \quad (1)$$

with hopping integrals t_i obtained from the fit to experimental Fermi surfaces [10]. The corresponding values of t_i (in eV) for the Ta system are $t_0 = -0.027$, $t_1 = 0.199$, $t_2 = 0.221$, $t_3 = 0.028$, $t_4 = 0.013$ for the band forming barrels around Γ and K points and $t_0 = 0.407$, $t_1 = 0.114$, $t_2 = 0.444$, $t_3 = -0.033$, $t_4 = 0.011$ for the band forming "bones". For the Nb system, $t_0 = 0.0003$, $t_1 = 0.0824$, $t_2 = 0.1667$, $t_3 = 0.0438$, $t_4 = 0.0158$ for the band forming smaller cylinders and $t_0 = 0.1731$, $t_1 = 0.1014$, $t_2 = 0.2268$, $t_3 = 0.037$, $t_4 = -0.0048$ for the band forming larger cylinders. These bands are used in the calculations in what follows.

3. ELECTRON SCATTERING ON A CDW

3.1. Commensurate CDW phase

We consider a schematic picture of the first Brillouin zone for a two-dimensional hexagonal lattice, shown in Fig. 3. In the hexagonal structures under study, the commensurate CDW vector is $\mathbf{Q} = \frac{2}{3}\Gamma M$, which corresponds to tripling the lattice period. Scattering an electron by this commensurate CDW vector returns the electron to an equivalent point after triple scattering: $\epsilon(\mathbf{k} + 3\mathbf{Q}) = \epsilon(\mathbf{k})$. Moreover, there are in fact six equivalent scattering vectors for hexagonal structures: $\mathbf{Q}_1 = (\frac{2}{3}, \frac{2}{3\sqrt{3}})\pi$, $\mathbf{Q}_2 = (\frac{2}{3}, \frac{2}{3\sqrt{3}})\pi$, $\mathbf{Q}_3 = (-\frac{2}{3}, \frac{2}{3\sqrt{3}})\pi$, and $\bar{\mathbf{Q}}_l = -\mathbf{Q}_l$ $(l = 1, 2, 3)$. Maxima of the Lindhardt function, calculated in Refs. [3, 10], are observed on these vectors $\mathbf{Q}$. In addition, the Lindhardt function shows pronounced maxima [3, 10] for the vectors $\mathbf{X} = \frac{1}{2}\Gamma K$ ($\mathbf{X}_1 = (\frac{2}{3}, 0)\pi$, $\mathbf{X}_2 = (\frac{1}{3}, \frac{1}{\sqrt{3}})\pi$, $\mathbf{X}_3 = (-\frac{1}{3}, \frac{1}{\sqrt{3}})\pi$, and $\bar{\mathbf{X}}_l = -\mathbf{X}_l$ $(l = 1, 2, 3)$), which appear as sums of the scattering vectors $\mathbf{Q}$ (see Table of momentum summation).

An electron with momentum $\mathbf{k}$ is therefore scattered by any of thirteen different momenta (see Table): $\mathbf{0}$, preserving its initial momentum $\mathbf{k}$; and $\mathbf{Q}$ ($\mathbf{Q}_l$ and $\bar{\mathbf{Q}}_l$); and $\mathbf{X}$ ($\mathbf{X}_l$ and $\bar{\mathbf{X}}_l$). In the one-band case, to find the diagonal Green's function of an electron $G(\mathbf{k}, \mathbf{k})$ and twelve off-diagonal ($G(\mathbf{k}\pm\mathbf{Q}_l, \mathbf{k})$ and $G(\mathbf{k}\pm\mathbf{X}_l, \mathbf{k})$) single-electron Green's functions, we therefore have to solve the system of thirteen linear equations (17) (see the Appendix). Such an approach can be generalized to a multiple-band case under the simplifying assumption [11] that the intra- and interband CDW scattering amplitudes coincide (see the Appendix). Solving these equations, we can finally find the diagonal Green's function $G^{ij}(\mathbf{k}, \mathbf{k})$ (where $i, j = 1, 2$ are band indices) and

Table of scattering vectors summation

	$\mathbf{Q}_1$	$\mathbf{Q}_2$	$\mathbf{Q}_3$	$\bar{\mathbf{Q}}_1$	$\bar{\mathbf{Q}}_2$	$\bar{\mathbf{Q}}_3$
$\mathbf{Q}_1$	$\bar{\mathbf{Q}}_1$	$\mathbf{X}_2$	$\mathbf{Q}_2$	0	$\bar{\mathbf{Q}}_3$	$\bar{\mathbf{X}}_1$
$\mathbf{Q}_2$	$\mathbf{X}_2$	$\bar{\mathbf{Q}}_2$	$\mathbf{X}_3$	$\mathbf{Q}_3$	0	$\mathbf{Q}_1$
$\mathbf{Q}_3$	$\mathbf{Q}_2$	$\mathbf{X}_3$	$\bar{\mathbf{Q}}_3$	$\bar{\mathbf{X}}_3$	$\bar{\mathbf{Q}}_1$	0
$\bar{\mathbf{Q}}_1$	0	$\mathbf{Q}_3$	$\bar{\mathbf{X}}_1$	$\mathbf{Q}_1$	$\bar{\mathbf{X}}_2$	$\bar{\mathbf{Q}}_2$
$\bar{\mathbf{Q}}_2$	$\bar{\mathbf{Q}}_3$	0	$\bar{\mathbf{Q}}_1$	$\bar{\mathbf{X}}_2$	$\mathbf{Q}_2$	$\bar{\mathbf{X}}_3$
$\bar{\mathbf{Q}}_3$	$\mathbf{X}_1$	$\mathbf{Q}_1$	0	$\bar{\mathbf{Q}}_2$	$\bar{\mathbf{X}}_3$	$\mathbf{Q}_3$

	$\mathbf{Q}_1$	$\mathbf{Q}_2$	$\mathbf{Q}_3$	$\bar{\mathbf{Q}}_1$	$\bar{\mathbf{Q}}_2$	$\bar{\mathbf{Q}}_3$
$\mathbf{X}_1$	$\bar{\mathbf{Q}}_2$	$\bar{\mathbf{Q}}_1$	$\mathbf{Q}_1$	$\bar{\mathbf{Q}}_3$	$\mathbf{Q}_3$	$\mathbf{Q}_2$
$\mathbf{X}_2$	$\mathbf{Q}_3$	$\bar{\mathbf{Q}}_3$	$\bar{\mathbf{Q}}_2$	$\mathbf{Q}_2$	$\mathbf{Q}_1$	$\bar{\mathbf{Q}}_1$
$\mathbf{X}_3$	$\bar{\mathbf{Q}}_2$	$\bar{\mathbf{Q}}_1$	$\mathbf{Q}_1$	$\bar{\mathbf{Q}}_3$	$\mathbf{Q}_3$	$\mathbf{Q}_2$
$\bar{\mathbf{X}}_1$	$\mathbf{Q}_3$	$\bar{\mathbf{Q}}_3$	$\bar{\mathbf{Q}}_2$	$\mathbf{Q}_2$	$\mathbf{Q}_1$	$\bar{\mathbf{Q}}_1$
$\bar{\mathbf{X}}_2$	$\bar{\mathbf{Q}}_2$	$\bar{\mathbf{Q}}_1$	$\mathbf{Q}_1$	$\bar{\mathbf{Q}}_3$	$\mathbf{Q}_3$	$\mathbf{Q}_2$
$\bar{\mathbf{X}}_3$	$\mathbf{Q}_3$	$\bar{\mathbf{Q}}_3$	$\bar{\mathbf{Q}}_2$	$\mathbf{Q}_2$	$\mathbf{Q}_1$	$\bar{\mathbf{Q}}_1$

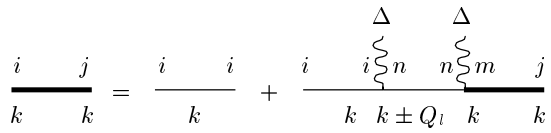

Fig. 4. Diagrammatic representation of the diagonal Green's function in the two-wave approximation for electron scattering on a CDW

the corresponding spectral function

$$A(E,\mathbf{k}) = -\frac{1}{\pi}\,\mathrm{Im}\sum_i G^{ii}(\mathbf{k},\mathbf{k}) \tag{2}$$

determining the effective electron dispersion.

3.2. Incommensurate CDW phase

It was noted above that at the temperature $T = 90$ K, 2H-$TaSe_2$ (and 2H-$NbSe_2$ at 33.5 K) undergoes a phase transition into the incommensurate CDW phase with the scattering vector $\mathbf{Q} \sim 0.58$–$0.6\Gamma M$. Similarly to the commensurate case discussed above, this vector corresponds to six independent scattering vectors $\mathbf{Q}_l, \bar{\mathbf{Q}}_l$, $l = 1,2,3$. We consider single scattering of an electron with momentum $\mathbf{k}$ near the FS by the vector $\mathbf{Q}(\mathbf{Q}_l, \bar{\mathbf{Q}}_l)$. For general values of $\mathbf{k}$, this scattering act moves the electron quite far away from the FS; the only exception is an electron in the vicinity of the "hot spots" where $\epsilon(\mathbf{k}+\mathbf{Q}) = \epsilon(\mathbf{k})$. Most probable among the multiple scattering processes is the successive scattering by vectors $\mathbf{Q}_l$ and $\bar{\mathbf{Q}}_l$ because the scattered electron then returns to the initial point with the momentum $\mathbf{k}$ close to the Fermi surface. In what follows, we therefore work in the so-called two-wave approximation, when the scattering act consists of two successive scattering processes by vectors $\mathbf{Q}_l$ and $\bar{\mathbf{Q}}_l$. Assuming that the scattering amplitude is the same for intra- and interband transitions, we obtain the diagonal Green's function in the form (the corresponding diagram representation is given in Fig. 4):

$$G^{ij}(\mathbf{k},\mathbf{k}) = g^i(\mathbf{k})\delta_{ij} + g^i(\mathbf{k})\Sigma\sum_m G^{mj}(\mathbf{k},\mathbf{k}), \tag{3}$$

where $\Sigma = \Delta^2\sum_{jl}(g^j(\mathbf{k}+\mathbf{Q}_l)+g^j(\mathbf{k}-\mathbf{Q}_l))$ and $g^j(\mathbf{k}) = \frac{1}{E-\epsilon_j(\mathbf{k})+i\delta}$ is the bare retarded Green's function for the nth band. Summing Eq. (3) over i yields

$$\sum_i G^{ij}(\mathbf{k},\mathbf{k}) = \frac{g^j(\mathbf{k})}{1-\Sigma\sum_i g^i(\mathbf{k})}. \tag{4}$$

Then using Eq. (3) again, we obtain

$$G^{ij}(\mathbf{k},\mathbf{k}) = g^i(\mathbf{k})\delta_{ij} + \frac{g^i(\mathbf{k})\Sigma g^j(\mathbf{k})}{1-\Sigma\sum_i g^i(\mathbf{k})}, \tag{5}$$

which yields spectral function (2) in the case of incommensurate CDW scattering.

3.3. CDW pseudogap fluctuations

Above the temperature of the incommensurate CDW transition, there is no long-range charge ordering, but due to low-dimensionality of the system, there are rather well developed short-range order CDW fluctuations with a finite correlation length ξ and the characteristic wave-vector $\mathbf{Q}$ that rather rapidly becomes commensurate with $\mathbf{Q} = \frac{2}{3}\Gamma M$ [4] as the temperature decreases. In analogy to the incommensurate electron–CDW scattering, we use the two-wave approximation with the pair of vectors $(\mathbf{Q}_l, \bar{\mathbf{Q}}_l)$. Diagrammatically, such scattering processes are show in Fig. 5, where three types of interaction lines correspond to three characteristic transfer momenta $l = 1,2,3$.

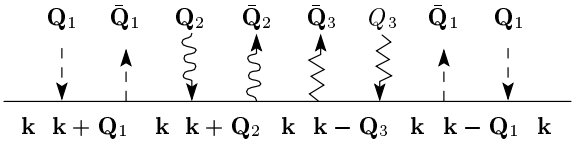

Fig. 5. Example of a diagram with multiple scattering on a CDW. The dashed, wavy, and zig-zag incoming lines respectively correspond to scattering on $\mathbf{Q}_1$, $\mathbf{Q}_2$, and $\mathbf{Q}_3$, and the corresponding outgoing lines, to $\bar{\mathbf{Q}}_1$, $\bar{\mathbf{Q}}_2$, and $\bar{\mathbf{Q}}_3$

We assume the fluctuations to be Gaussian. Then averaging over such fluctuations corresponds to all possible interconnections of the incoming and outgoing interaction lines of the same type [12–14], producing appropriate effective interactions, assumed to be of the form discussed in these works. For high enough temperatures, we can neglect the dynamics of fluctuations and average over a static random field of Gaussian pseudogap fluctuations [12–14].

We note that the number of different diagrams is defined by the product of the number of ways to interconnect vertices of types 1, 2, and 3. Because only outgoing and incoming lines of each type can be connected, the combinatorics corresponds to the incommensurate case [12]. Following Refs. [12–14], we use the basic property of the diagrams of this model: any diagram with crossing interaction lines is equal to some noncrossing diagram of the same order. Hence, only noncrossing diagrams can be considered, while contributions of all diagrams can be accounted for by combinatorial prefactors. For each type of interaction lines (1,2,3), we have its own incommensurate combinatorial prefactors, the same as in Refs. [12, 13].

Recurrent procedure for the Green's function: single-band case

Using straightforward generalization of the approach in Refs. [12, 13], the one-electron Green's function can be obtained in the single-band case via a recurrent procedure, which is shown diagrammatically in Fig. 6. There, n_l is the number of interaction lines of type l surrounding the "bare" electron line. Analytically, this procedure can be written as

$$G^{-1}_{n_1,n_2,n_3}(\mathbf{k}) = g^{-1}_{n_1,n_2,n_3}(\mathbf{k}) - \Sigma_{n_1+1,n_2,n_3} - \Sigma_{n_1,n_2+1,n_3} - \Sigma_{n_1,n_2,n_3+1}, \quad (6)$$

where n_1, n_2, n_3 are even and

$$\Sigma_{n_1+1,n_2,n_3} = \Delta^2 s(n_1+1) \times \times \left[G_{n_1+1,n_2,n_3}(\mathbf{k}+\mathbf{Q_1}) + G_{n_1+1,n_2,n_3}(\mathbf{k}-\mathbf{Q_1})\right]. \quad (7)$$

The other self-energies Σ in Eq. (6) can be found similarly to (7), but n_2 or n_3 should be increased by one and the vectors $\mathbf{Q_2}$ or $\mathbf{Q_3}$ should be added (subtracted) to (from) $\mathbf{k}$, while

$$G^{-1}_{n_1+1,n_2,n_3}(\mathbf{k}\pm\mathbf{Q_1}) = g^{-1}_{n_1+1,n_2,n_3}(\mathbf{k}\pm\mathbf{Q_1}) - \Sigma_{n_1+2,n_2,n_3}, \quad (8)$$

and

$$\Sigma_{n_1+2,n_2,n_3} = \Delta^2 s(n_1+2) G_{n_1+2,n_2,n_3}(\mathbf{k}). \quad (9)$$

Here,

$$g_{n_1,n_2,n_3}(\mathbf{k}) = \frac{1}{E - \epsilon(\mathbf{k}) + inv(\mathbf{k})\kappa}, \quad (10)$$

$\kappa = 1/\xi$ is the inverse correlation length of pseudogap fluctuations, $n = n_1 + n_2 + n_3$, $v(\mathbf{k}) = |v_x(\mathbf{k}) + v_y(\mathbf{k})|$, and $v_{x,y}(\mathbf{k}) = \frac{\partial\epsilon(\mathbf{k})}{\partial k_{x,y}}$ are projections of quasiparticle velocities.

For incommensurate fluctuations, the combinatorial prefactors are

$$s(n) = \begin{cases} \dfrac{n+1}{2} & \text{for odd } k, \\ \dfrac{n}{2} & \text{for even } k. \end{cases} \quad (11)$$

This recurrent procedure is applied in analogy with Refs. [12, 13]. At the first step, we take large enough $n = n_1 + n_2 + n_3$, for example even, and assume that all Green's functions G_{n_1,n_2,n_3} with even n_1, n_2, n_3, such that $n = n_1 + n_2 + n_3$ are equal to zero. From Eq. (9), we then find that all Σ_{n_1,n_2,n_3} for the same indices are also equal to zero. Then using the recurrent procedure, we can obtain *all* new values for G_{n_1,n_2,n_3} with even n_1, n_2, n_3, such that $n_1 + n_2 + n_3 = n - 2$, and repeat the procedure until we obtain the physical Green's function

$$G(\mathbf{k}) = G_{0,0,0}(\mathbf{k}). \quad (12)$$

Multiple-band pseudogap model for quasi-two-dimensional hexagonal structures

In hexagonal diselenides $TaSe_2$ and $NbSe_2$, as we have seen, the Fermi level is crossed by two bands. Hence, our recurrent procedure should be generalized for the case of multiple bands. We follow Ref. [11], devoted to the description of possible pseudogap behavior in iron-based superconductors, and assume that the intra- and interband pseudogap scattering amplitudes are identical. This simplifies the analysis and the recurrent procedure for diagonal elements (with respect

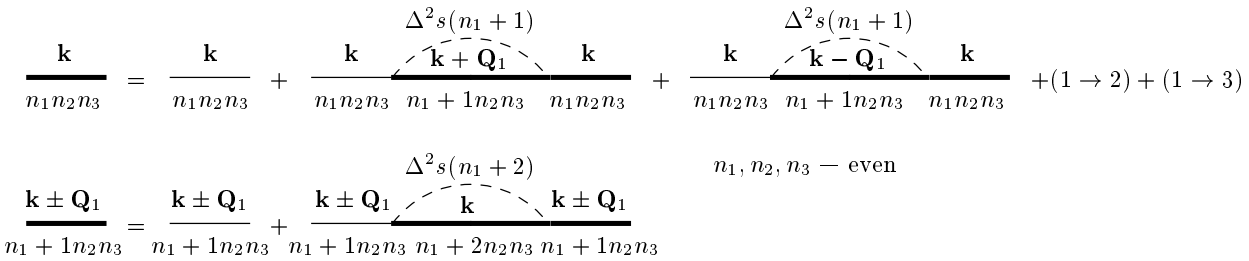

Fig. 6. Diagram representation of the Green's function in the single-band pseudogap model for two-dimensional hexagonal systems; $(1 \to 2)$ denotes the last two terms, where the substitutions $Q_1 \to Q_2$ and $n_1 + 1 \to n_2 + 1$ should be done

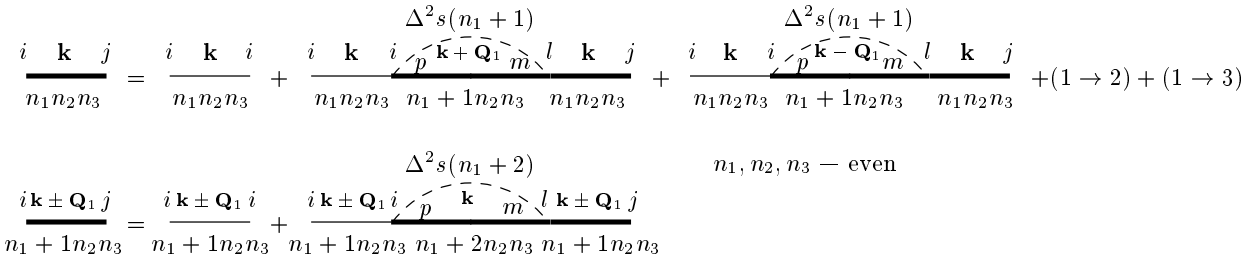

Fig. 7. Diagram representation of the Green's function in the multiband pseudogap model for two-dimensional hexagonal systems

to band indices) of the general matrix Green's function G^{ij} can be drawn diagrammatically as in Fig. 7. For our two-band model, each of the band indices ranges over two possible values, and summation is performed over all possible values of indices p, m, l in the vertices (Fig. 7). Therefore, the self-energy in these diagrams has no dependence on band indices at all, and we can obtain the recurrent procedure for $G_{n_1,n_2,n_3} = \sum_{i,j} G^{ij}_{n_1,n_2,n_3}$, which is identical to Eqs. (6)–(9) in the single-band case, with the only replacement

$$g_{n_1,n_2,n_3}(\mathbf{k}) = \sum_i g^j_{n_1,n_2,n_3}(\mathbf{k}) = \\ = \sum_j \frac{1}{E - \epsilon_j(\mathbf{k}) + i n v_j(\mathbf{k})\kappa}, \quad n = n_1 + n_2 + n_3. \quad (13)$$

At the end of the procedure, we define the physical matrix Green's function as

$$G^{ij}(\mathbf{k}) = g^i_{0,0,0}(\mathbf{k})\delta_{ij} + \frac{g^i_{0,0,0}(\mathbf{k})\Sigma g^j_{0,0,0}(\mathbf{k})}{1 - \Sigma g_{0,0,0}(\mathbf{k})}, \quad (14)$$

where $\Sigma = \Sigma_{1,0,0} + \Sigma_{0,1,0} + \Sigma_{0,0,1}$. This Green's function allows finding spectral function (2) in the presence of CDW pseudogap fluctuations.

4. RESULTS AND DISCUSSION

In our calculations, we used a rather typical estimate of CDW potential $\Delta = 0.05$ eV, and we assumed the value $\xi = 10a$ (where a is the lattice spacing) for the correlations length of pseudogap fluctuations. To mimic the experimental ARPES resolution, we broadened our spectral functions with a Lorentzian of the width $\gamma = 0.03$ eV, which practically means that we made the substitution $E \to E + i\gamma$ throughout the calculation.

In Fig. 8, we show spectral function maps along high-symmetry directions with k_z=0 for 2H-$TaSe_2$. The upper panel shows a spectral function map for the incommensurate pseudogap phase obtained within our pseudogap model. In general, it resembles the bare "experimental" dispersions plotted in Fig. 2. But we here see some additional broadening of the initial spectra. These broadened regions of spectral functions with a lower intensity represent regions of pseudogap formation. Why do we speak about regions? In contrast to cuprates [15], where we have a finite and rather small number of "hot spots", we here have virtually infinitely many "hot spots", and it is the interplay between all of them that leads to the formation of such regions. But still the dispersion here does not have any obvious discontinuities.

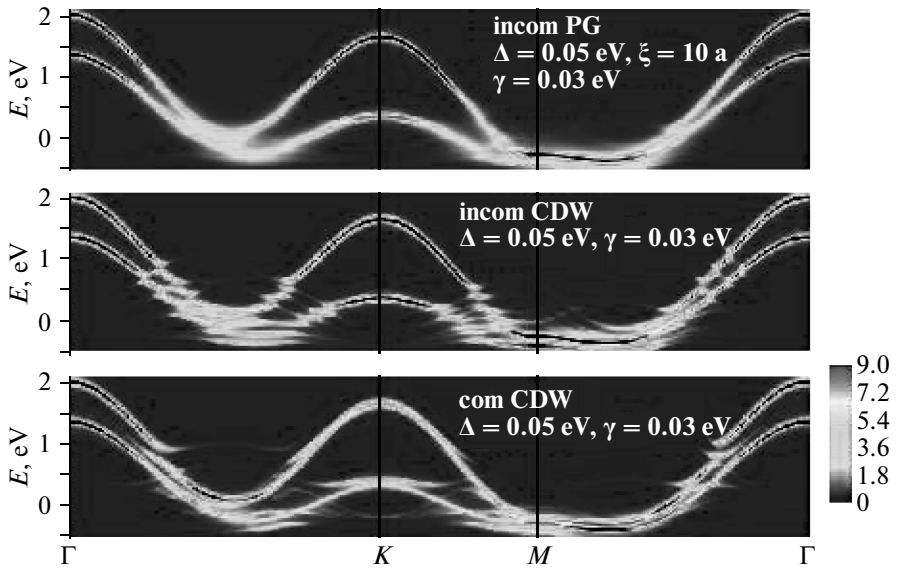

Fig. 8. Spectral functions of 2H-$TaSe_2$. The upper panel: the incommensurate pseudogap phase; the middle panel: the incommensurate CDW phase, the lower panel: commensurate CDW phase

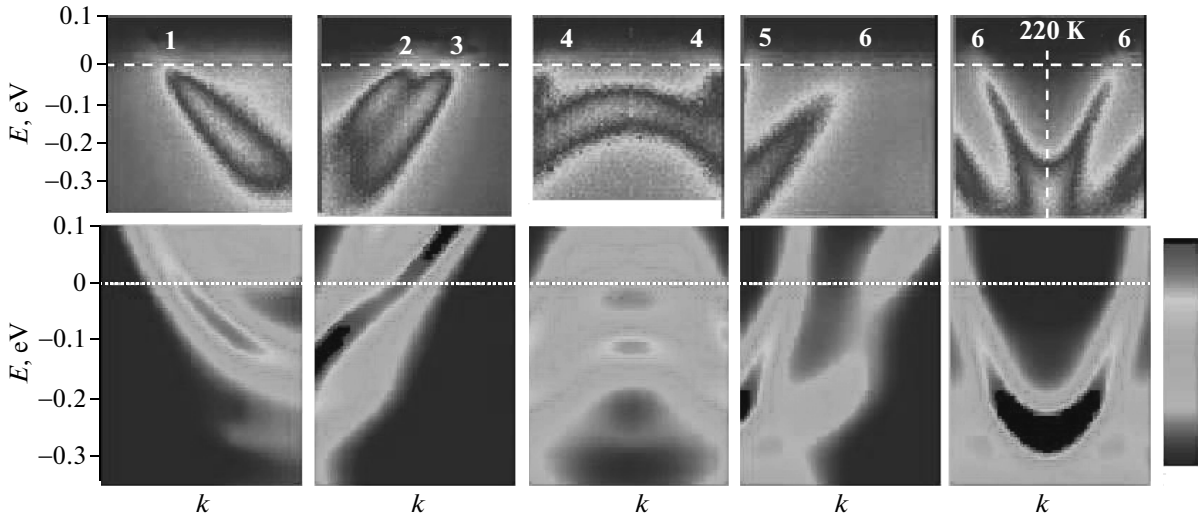

Fig. 9. Spectral functions for the incommensurate pseudogap phase along the cuts shown in Fig. 1*c*

The middle panel in Fig. 8 displays the case of the incommensurate CDW phase. We see that the regions previously covered with a pseudogap have clear discontinuities — gaps and also many shadow bands. When we pass further to the commensurate CDW phase (the lower panel in Fig. 8), those gaps become even stronger and we can see much more pronounced shadow bands.

Figures 9–11 show spectral function maps in the vicinity of the Fermi level along the cuts shown in Fig. 1*c*. In all figures, the upper row represents experimental data in Ref. [4], while the lower one shows our theoretical results. Generally speaking, in all phases — the incommensurate pseudogap Fig. 9, the incommensurate CDW Fig. 10, and the commensurate CDW Fig. 11 — we obtain a rather good qualitative agreement of the theory and the experiment for the number of bands crossing the Fermi level, their position, and relative intensity.

In Fig. 12, we compare the experimental and theoretical Fermi surfaces for 2H-$TaSe_2$. In the middle part of Fig. 12, we show the experimental ARPES data from Ref. [4]. The data at 180 K correspond to the pseudo-

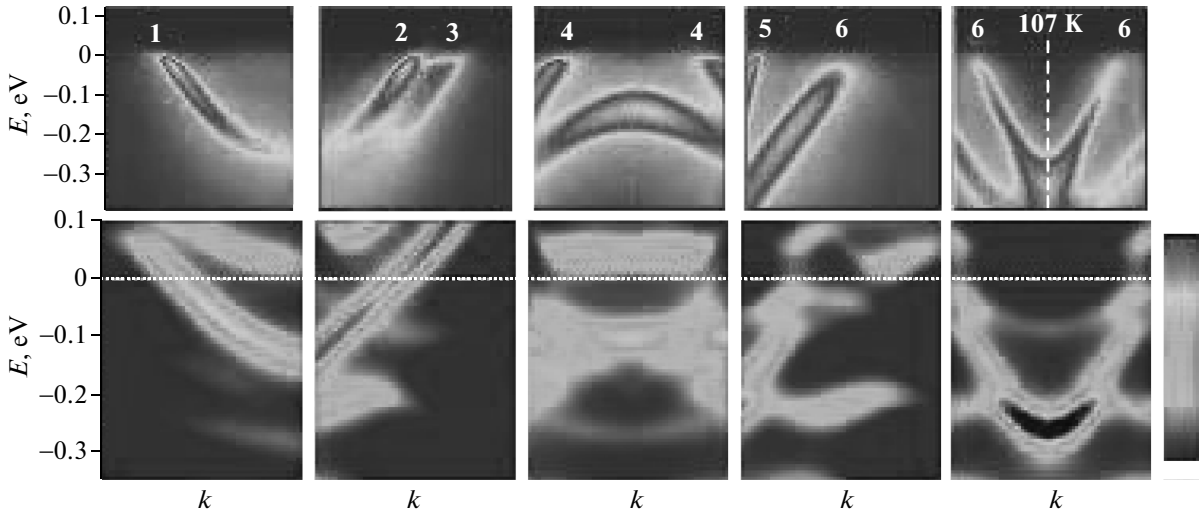

Fig. 10. The same as in Fig. 9 but for the incommensurate CDW phase

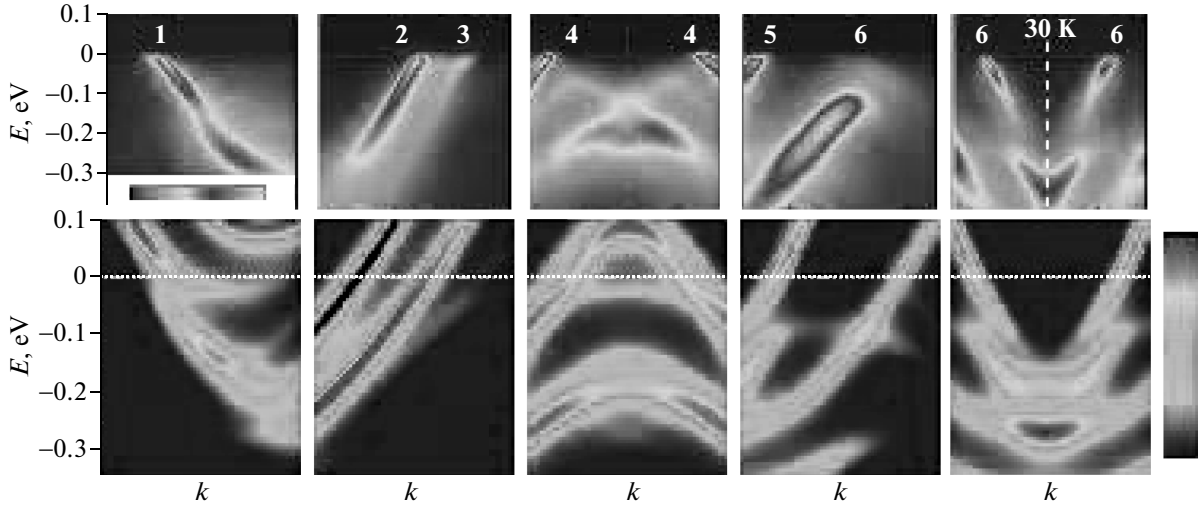

Fig. 11. The same as in Fig. 9 but for the commensurate CDW phase

gap phase, and those at 30 K are for the commensurate CDW phase.

The upper panel in Fig. 12, shows our theoretical Fermi surface in the incommensurate pseudogap regime for 2H-$TaSe_2$. In general, it more or less resembles the LDA Fermi surface in Fig. 1*c*. But there are obvious signatures of partial destruction of the Fermi surface sheets. Namely, a cylinder around the K point and "bones" along the K–M direction are partially smeared. It is seen that this picture agrees well with the experimental ARPES data in Ref. [3, 4].

For the commensurate CDW phase (the lower panel in Fig. 12), the Fermi surface stays close to that obtained in the LDA and shown in Fig. 1*c*. In contrast to the incommensurate pseudogap phase, the Fermi surface sheets are here sharper in both experiment and theory. The cylinder around the K point is now continuous. In the middle of the "bones", we observe the start of formation of small triangles, shown in the center of the middle panel. In the commensurate CDW phase of 2H-$TaSe_2$, we therefore again obtain an overall agreement between theory and experiment.

In Fig. 13, we compare experimental (middle panel) and theoretical (lower and upper panels) Fermi surfaces for 2H-$NbSe_2$. Experimental data on the Fermi surface are available only for the commensurate CDW

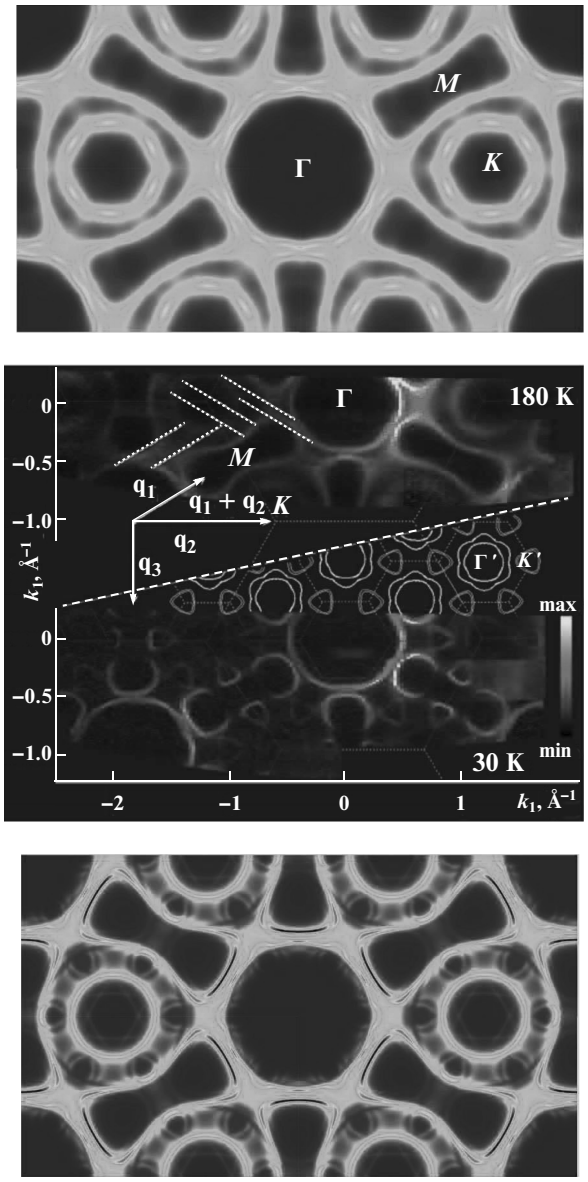

Fig. 12. Comparison of experimental and theoretical Fermi surfaces for 2H-$TaSe_2$. The upper panel: the theoretical Fermi surface for the pseudogap CDW phase; the middle panel: a joint picture of the experimental data on the pseudogap phase (upper part) and the commensurate CDW phase (lower part). The lower panel: the theoretical Fermi surface for the commensurate CDW phase

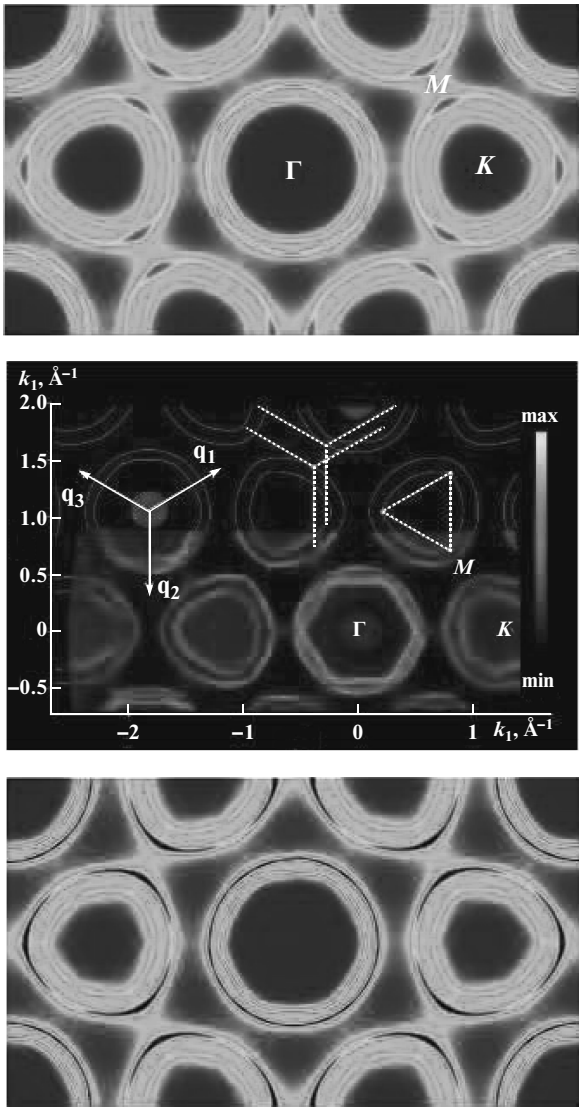

Fig. 13. Comparison of experimental and theoretical Fermi surfaces for 2H-$NbSe_2$. The upper panel: the theoretical Fermi surface for the pseudogap CDW phase; the middle panel: a joint picture of the experimental data on the LDA Fermi surface (upper part) and the commensurate CDW phase (lower part). The lower panel: the theoretical Fermi surface for the commensurate CDW phase

phase [5]. We can therefore compare these with the theoretical picture shown in lower panel in Fig. 13. In general, both Fermi surfaces resemble those in Fig. 1*b*. Taking the electron scattering on a commensurate CDW into account leads to small regions of Fermi surface destruction, namely, along the Γ–K and K–M directions. If there exists an incommensurate pseudogap phase for 2H-$NbSe_2$ at sufficiently high temperatures, its Fermi surface is not changed much by pseudogap fluctuations, as can be seen in the upper panel in Fig. 13.

5. CONCLUSION

To conclude, we have presented theoretical results on the electronic structure of two-dimensional diselenides 2H-$TaSe_2$ and 2H-$NbSe_2$ within different CDW phases.

First of all, we formulated a theoretical approach to account for multiple scattering of electrons on different CDW types, also in the multiple-band case. We next investigated spectral functions and Fermi surfaces for the pseudogap, incommensurate CDW, and commensurate CDW phases. The calculated theoretical spectral functions for the pseudogap phase demonstrate "hot regions" where the spectral function is additionally broadened. In incommensurate CDW and commensurate CDW phases, in place of these "hot regions", we obtained the opening of the number of gaps at the intersections with rather pronounced "shadow bands". Comparing experimental and theoretical Fermi surfaces in the pseudogap phase, we observe rather clear signs of partial Fermi surface destruction with formation of a number of typical "Fermi arcs", separated by pseudogap regions. In the commensurate CDW phase, Fermi surfaces are rather similar to those in the initial LDA picture, with quite small features due to CDW. The overall agreement between theory and ARPES experiments is rather satisfactory.

We thank S. V. Borisenko for his interest and helpful discussions. This work was supported in part by the RFBR grant 11-02-00147 and was performed in the framework of Programs of Fundamental Research of the Russian Academy of Sciences (RAS) "Quantum physics of condensed matter" (UB RAS 09-II-2-1009) and of the Physics Division of RAS "Strongly correlated electrons in solid states" (UB RAS 09-T-2-1011).

APPENDIX

Scattering on an commensurate CDW

One-band scattering

We first consider the single-band case with a "bare" electron spectrum $\epsilon(\mathbf{k})$. These "bare" electrons are scattered on the CDW potential written as

$$V(\mathbf{r}) = 2\Delta \sum_{l=1}^{3} \cos \mathbf{Q}_l \mathbf{r}. \tag{15}$$

The "bare" retarded Green's function is

$$g(\mathbf{k}) = \frac{1}{E - \epsilon(\mathbf{k}) + i\delta}. \tag{16}$$

We introduce the short notation $g(\mathbf{k}) = g$, $g(\mathbf{k}+\mathbf{Q}_l) = f_l$, $g(\mathbf{k}-\mathbf{Q}_l) = f_{\bar{l}}$, $g(\mathbf{k}+\mathbf{X}_l) = \phi_l$, and $g(\mathbf{k}-\mathbf{X}_l) = \phi_{\bar{l}}$. For the diagonal Green's function $G = G(\mathbf{k},\mathbf{k})$ and twelve off-diagonal ones ($F_l = G(\mathbf{k}+\mathbf{Q}_l,\mathbf{k})$, $F_{\bar{l}} = G(\mathbf{k}-\mathbf{Q}_l,\mathbf{k})$, $\Phi_l = G(\mathbf{k}+\mathbf{X}_l,\mathbf{k})$, $\Phi_{\bar{l}} = G(\mathbf{k}-\mathbf{X}_l,\mathbf{k})$), we then obtain the system of thirteen linear equations (see Table of scattering vector summation):

$$\begin{aligned}
G &= g + g\Delta F,\\
F_1 &= f_1\Delta(F_{\bar{1}} + \Phi_2 + F_2 + G + F_{\bar{3}} + \Phi_1),\\
F_2 &= f_2\Delta(\Phi_2 + F_{\bar{2}} + \Phi_3 + F_3 + G + F_1),\\
F_3 &= f_3\Delta(F_2 + \Phi_3 + F_{\bar{3}} + \Phi_{\bar{1}} + F_{\bar{1}} + G),\\
F_{\bar{1}} &= f_{\bar{1}}\Delta(G + F_3 + \Phi_{\bar{1}} + F_1 + \Phi_{\bar{2}} + F_{\bar{2}}),\\
F_{\bar{2}} &= f_{\bar{2}}\Delta(F_{\bar{3}} + G + F_{\bar{1}} + \Phi_{\bar{2}} + F_2 + \Phi_{\bar{3}}),\\
F_{\bar{3}} &= f_{\bar{3}}\Delta(\Phi_1 + F_1 + G + F_{\bar{2}} + \Phi_{\bar{3}} + F_3),\\
\Phi_l &= \phi_l\Delta F, \quad \Phi_{\bar{l}} = \phi_{\bar{l}}\Delta F,
\end{aligned} \tag{17}$$

where $F = \sum_{l=1}^{3}(F_l + F_{\bar{l}})$.

Solving Eqs. (17) yields the diagonal Green's function $G = G(\mathbf{k},\mathbf{k})$:

$$G = gK; \quad K = \frac{1 - \alpha\beta - a(\beta+1) - b(\alpha+1)}{1-\alpha\beta-a(\beta+1)-b(\alpha+1)-g\Delta[\alpha(\beta+1)+\beta(\alpha+1)]}, \tag{18}$$

where $\alpha = \Delta(f_2 + f_{\bar{1}} + f_{\bar{3}})$, $\beta = \Delta(f_1 + f_3 + f_{\bar{2}})$, $a = \Delta^2[f_{\bar{1}}(\phi_{\bar{1}} + \phi_{\bar{2}}) + f_2(\phi_2 + \phi_3) + f_{\bar{3}}(\phi_{\bar{3}} + \phi_1)]$, and $b = \Delta^2[f_1(\phi_1 + \phi_2) + f_3(\phi_3 + \phi_{\bar{1}}) + f_{\bar{2}}(\phi_{\bar{2}} + \phi_{\bar{3}})]$.

Multiband scattering

Following the approach in Ref. [11], we assume that the CDW scattering amplitude Δ is identical for intra- and interband transitions. We introduce the short notations $g^i = g^i(\mathbf{k}) = \frac{1}{E-\epsilon_i(\mathbf{k})+i\delta}$, $f^i_{l(\bar{l})} = g^i(\mathbf{k}\pm\mathbf{Q}_l)$, and $\phi^i_{l(\bar{l})} = g^i(\mathbf{k}\pm\mathbf{X}_l)$, where i is the band index. The diagonal and off-diagonal Green's functions have additional band indices. The rest of the notation is the same as in the single-band case. For the diagonal Green's function, in analogy with first equation of system (17), we can obtain

$$G^{ij} = g^i\delta_{ij} + g^i\Delta \sum_m \sum_{l=1}^{3}(F^{mj}_l + F^{mj}_{\bar{l}}). \tag{19}$$

Introducing $G^j = \sum_i G^{ij}$, $F^j_{l(\bar{l})} = \sum_i F^{ij}_{l(\bar{l})}$, $\Phi^j_{l(\bar{l})} = \sum_i \Phi^{ij}_{l(\bar{l})}$, $g = \sum_i g^i$, $f_{l(\bar{l})} = \sum_i f^i_{l(\bar{l})}$, and $\phi_{l(\bar{l})} = \sum_i \phi^i_{l(\bar{l})}$ and summing Eq. (19) over i, we obtain

$$G^j = g^j + g\Delta \sum_{l=1}^{3}(F^j_l + F^j_{\bar{l}}). \tag{20}$$

The other twelve equations for $F^j_{l(\bar{l})}$ and $\Phi^j_{l(\bar{l})}$ are completely equivalent to the corresponding one-band equations (17). Hence, we immediately obtain

$$G^j = g^j K, \tag{21}$$

where K is defined in Eq. (18). But the quantities g, $f_{l(\bar{l})}$, and $\phi_{l(\bar{l})}$ are now summed over all band indices. From Eqs. (19) and (20), using Eq. (21), we finally obtain

$$G^{ij} = g^i\delta_{ij} + g^i\frac{G^j - g^j}{g} = g^i\delta_{ij} + \frac{g^i g^j}{g}(K-1), \tag{22}$$

which allows calculating spectral function (2) with the account of scattering on a commensurate CDW.

REFERENCES

1. J. A. Wilson, F. J. Di Salvo, and S. Mahajan, Adv. Phys. **24**, 117 (1975).
2. D. E. Moncton, J. D. Axe, and F. J. Di Salvo, Phys. Rev. Lett. **34**, 734 (1975); Phys. Rev. B **16**, 801 (1977).
3. D. S. Inosov, V. B. Zabolotnyy, D. V. Evtushinsky et al., New J. Phys. **10**, 125027 (2008).
4. S. V. Borisenko, A. A. Kordyuk, A. N. Yaresko et al., Phys. Rev. Lett. **100**, 196402 (2008).
5. S. V. Borisenko, A. A. Kordyuk, V. B. Zabolotnyy et al., Phys. Rev. Lett. **102**, 166402 (2009).
6. O. K. Andersen, Phys. Rev. B **12**, 3060 (1975); O. Gunnarsson, O. Jepsen, and O. K. Andersen, Phys. Rev. B **27**, 7144 (1983); O. K. Andersen and O. Jepsen, Phys. Rev. Lett. **53**, 2571 (1984).
7. R. A. Bromley, Phys. Rev. Lett. **29**, 357 (1972); L. F. Mattheiss, Phys. Rev. B **8**, 3719 (1973); G. Wexler and A. M. Wooley, J. Phys. C: Sol. St. Phys. **9**, 1185 (1976); R. Corcoran et al., J. Phys.: Condens. Matter **6**, 4479 (1994); H. E. Brauer et al., J. Phys.: Condens. Matter **13**, 9879 (2001); M.-T. Suzuki and H. Harima, Physica B **359–361**, 1180 (2004).
8. N. V. Smith, S. D. Kevan, and F. J. Di Salvo, J. Phys. C: Sol. St. Phys. **18**, 3175 (1985).
9. K. Rossnagel, E. Rotenberg, H. Koh, N. V. Smith, and L. Kipp, Phys. Rev. B **72**, 121103 (2005).
10. D. S. Inosov, D. V. Evtushinsky, V. B. Zabolotnyy et al., Phys. Rev. B **79**, 125112 (2009).
11. E. Z. Kuchinskii and M. V. Sadovskii, Pis'ma v ZhETF **91**, 729 (2010).
12. M. V. Sadovskii, Zh. Eksp. Teor. Fiz. **66**, 1720 (1974); **77**, 2070 (1979).
13. E. Z. Kuchinskii and M. V. Sadovskii, Zh. Eksp. Teor. Fiz. **115**, 1765 (1999).
14. J. Schmalian, D. Pines, and B. Stojkovic, Phys. Rev. Lett. **80**, 3839 (1998); Phys. Rev. B **60**, 667 (1999).
15. M. V. Sadovskii, Usp. Fiz. Nauk **171**, 539 (2001). Also in *Strings, Branes, Lattices, Networks, Pseudogaps, and Dust*, Scientific World, Moscow (2007), p. 357.